J. Iron Steel Res. Int. (2024) 31:121–133
https://doi.org/10.1007/s42243-022-00823-2

ORIGINAL PAPER

Distribution of oxide inclusions in H13 castings under super-gravity field with multi-stage rotation speeds

Shao-ying Li[1,2] · Xiao-jun Xi[3] · Xing-ming Zhao[4] · Han-jie Guo[1,2] · Jing Guo[1,2]

Received: 31 January 2022 / Revised: 21 March 2022 / Accepted: 4 April 2022 / Published online: 29 August 2022

Abstract

The 42 kg industrial H13 castings were prepared by different super-gravity fields with multi-rotation speeds, and the distribution of oxide inclusions in the castings was studied. In addition, the inward movement Reynolds number and inward movement time of oxide inclusions as well as the solidification time of molten steel at different positions in the castings were calculated to clarify the removal mechanism of oxide inclusions in super-gravity field. The results show that the large size (i.e., greater than 10 μm) oxide inclusions are mainly concentrated in the inner and outer parts of the super-gravity castings with constant rotation speed (500 r min^{-1}) and five-stage rotation speeds (500, 600, 750, 850, and 950 r min^{-1}), respectively, while there are no large oxide inclusions in the super-gravity castings with three-stage rotation speeds (500, 600, and 750 r min^{-1}). Although an increase in the particle size of inclusion and the rotation speed in super-gravity field is conducive to the increase in the inward movement Reynolds number of oxide inclusions and reduction in the inward movement time of oxide inclusions, it will reduce the local solidification time of molten steel. In the range of the rotation speed studied, the super-gravity field with three-stage rotation speeds has the best effect on the removal of inclusions in H13 molten steel.

Keywords Distribution · Oxide inclusion · H13 casting · Super-gravity field · Rotation speed

1 Introduction

H13 die steel is widely used in extrusion, die casting, hot forging, and other harsh working conditions, which require it to have the characteristics of high strength, high toughness, and high hardness at the same time [1, 2]. Oxide inclusions have a direct hazard to the mechanical properties of steel [3]. To eliminate this hazard, the removal of oxide inclusions has always been an ongoing concern. Many methods have been put forward to minimize the amount of oxide inclusions including electroslag remelting [4, 5], inclusion modification [6], gas stirring [7], ceramic filter [8], bubbling [9], and electromagnetic purification [10, 11]. Although these methods can remove inclusions, they have certain limitations for industrial production. For example, electroslag remelting has high production cost and is only suitable for producing high-end products [4]. Inclusion modification may cause nozzle blockage [12]. Gas stirring is only suitable for inclusions larger than 50 μm in size [13]. The treatment efficiency of gas stirring is low, leading to the difficulty in ensuring continuous production [14]. Therefore, it is necessary to develop the technology of removing inclusions with low cost, high efficiency, and strong operability.

As a process enhancement technology, super-gravity technology has the advantages of low cost, strong operability, and no pollution, which is applied in chemical process industry [15–17], electrochemical field [18, 19], and metallurgical field. Generally, metallurgical melts contain phases with different densities, and different phases

✉ Han-jie Guo
guohanjie@ustb.edu.cn

1 School of Metallurgical and Ecological Engineering, University of Science and Technology Beijing (USTB), Beijing 100083, China

2 Beijing Key Laboratory of Special Melting and Preparation of High-End Metal Materials, Beijing 100083, China

3 Beijing Beiye Functional Materials Corporation, Beijing 100192, China

4 Shandong Tianwu Forming Technology Co., Ltd., Liaocheng 252024, Shandong, China

can be separated or enriched under the action of super-gravity [20]. For example, Zhao et al. [21] studied the removal of impurity elements from aluminum melt with super-gravity, which make impurity elements Fe and Si segregate at the two ends of the sample along the direction of super-gravity, respectively. With the development of super-gravity technology in metallurgical field, the technology has been gradually used to the laboratory-scale experiments of the removal of inclusions in molten metal. Song et al. [22] studied the super-gravity separation of SiO_2 particles with a size of 50 μm from the aluminum melt weighing 20 g, which shows that the degree of separation of inclusions and melt increases with the increase in separation time. Li et al. [23] studied the separation of fine Al_2O_3 inclusions with the size less than 1 μm from molten steel weighing 300 g with super-gravity, and the effects of different gravity coefficients and time on separating the inclusions were investigated, which shows that the best removal rate of inclusions is up to 95.6% under the condition of gravity coefficient $G = 80$ and time $t = 15$ min. These experimental results show that the removal of inclusions in molten metal by super-gravity is feasible. It is worth noting that the ingot mass in these laboratory-scale experiments is small, and the cooling conditions during the experiment can be controlled. Obviously, in the process of industrial production for the removal of inclusions in molten metal by super-gravity, the mass of small ingot and the cooling condition during solidification cannot be completely controlled. Therefore, the study on the distribution mechanism of inclusions in industrial ingots solidified in super-gravity field is conducive to promoting the industrial application of the removal of inclusions in molten metal by super-gravity.

In this study, the super-gravity fields with different rotation speeds were applied to the solidification process of 42 kg industrial castings. The distribution and size of non-metallic inclusions in different castings were investigated. Simultaneously, the removal mechanism of non-metallic inclusions was discussed in terms of the movement trajectory and movement time of oxide inclusions and the solidification time of castings in super-gravity field.

2 Experimental details

The super-gravity H13 castings used in the study were prepared in a steel plant in northern China. The experimental process is shown in Fig. 1a and b. The molten metal (42 kg) and slag (8 kg) were poured into a rotating mold with a certain rotation speed. Here, the chemical composition of the slag is shown in Table 1. Before pouring, the temperature of the mixture of molten steel and slag is controlled in the range of 1650 ± 20 °C, which is

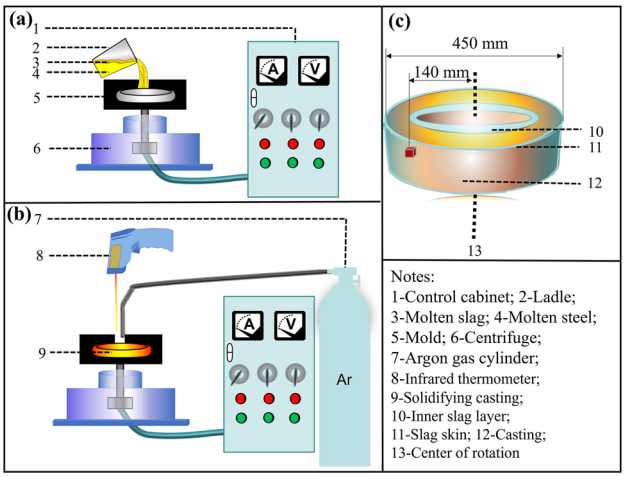

Fig. 1 Schematic diagram of super-gravity solidification experiment process. **a** Molten steel and slag are poured into mold; **b** super-gravity casting is solidifying; **c** solidified super-gravity casting

Table 1 Chemical composition of slag (wt.%)

CaO	SiO_2	MgO	Al_2O_3	CaF_2
8.2	4.0	18.3	8.2	61.3

measured using an infrared thermometer (IR-HOH, Beijing Duhelichuang Technology Co., Ltd., Beijing, China). The mixtures of molten steel and slag were completely poured into the mold within 10 s. Due to the density difference between molten slag and molten steel, a small amount of molten slag enters the mold in priority to the molten steel, and the molten slag entering the mold in priority forms a slag crust to prevent the adhesion of the casting and the mold. Then, the mixture of molten slag and steel enters the mold. Under the action of super-gravity, the centrifugal speed of the molten steel is greater than that of the molten slag, which causes the molten slag easy to accumulate to the center of rotation. Finally, the remaining molten slag is poured into the mold. Since the temperature of the molten slag is higher than that of the molten steel, a solidification field with high center temperature and low edge temperature is formed in the mold. Therefore, the shrinkage cavity in the casting can be supplemented in time to ensure the compactness of the casting. The solidified casting is shown in Fig. 1c.

Before super-gravity solidification, the content of the main elements in the steel was measured using a spark-optical emission spectrometer, and the contents of oxygen and nitrogen in the steel were analyzed with an oxygen and nitrogen hydrogen analyzer (TCH600, LECO, San Jose, CA, USA). The chemical composition control range of the sample is listed in Table 2. In order to determine the effect

Table 2 Chemical composition control range of H13 die steel (wt.%)

C	Si	Mn	Cr	Mo	V	O	N	Fe
0.46–0.51	0.8–0.9	0.3	4.5–4.6	1.2–1.4	0.9–1.0	≤ 0.004	≤ 0.012	Balance

Table 3 Rotation speed and time of each stage during super-gravity solidification

Casting	First stage		Second stage		Third stage		Fourth stage		Fifth stage	
	Speed/(r min^{-1})	Time/min	Speed/(r min^{-1})	Time/min	Speed/(r min^{-1})	Time/min	Speed/(r min^{-1})	Time/min	Speed/(r min^{-1})	Time/min
A	500	8.2								
B	500	0.2	600	4	750	4				
C	500	0.2	600	2	750	2	850	2	950	2

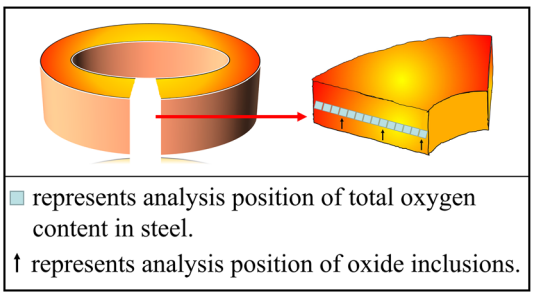

Fig. 2 Schematic diagram of sampling location for analysis of total oxygen content and oxide inclusions

of rotation speed of super-gravity field on the size and quantity of oxide inclusions and prevent other experimental conditions from interfering with the statistical results, the oxygen content in molten steel before super-gravity solidification was controlled within $(38 \pm 2) \times 10^{-6}$. The experimental parameters of the super-gravity experiments with different rotation speeds are shown in Table 3.

The total oxygen content at each position along the super-gravity direction on the cross section of the casting was analyzed, and the sampling position is shown in the blue square in Fig. 2. According to the oxygen content of sample at different positions on the cross section of different castings (see Sect. 3.2), the analysis position of oxide inclusions can be determined as shown by the black arrows in Fig. 2. The morphology of oxide inclusions was observed on a Geminisem 500 field emission scanning electron microscope, and the size and the number of the oxide inclusions in a square area with dimensions of 4 mm × 4 mm in the samples were analyzed with a ZEISS EVO18 scanning electron microscope (SEM) equipped with an ASPEX system.

3 Results

3.1 Types of oxide inclusions

H13 die steel is a medium-carbon alloy steel, and the alloying elements in the steel are easily combined with C, N, and O to generate oxides, carbonitrides, and carbides. The oxides are mainly magnesia–alumina spinel and magnesium oxide, as shown in Fig. 3a and b. Since the formation temperature of MgO is higher than that of (Ti, V) C, N, the phenomenon that MgO is surrounded by (Ti, V)C,N appears in Fig. 3b.

3.2 Size distribution of oxide inclusions

With the oxygen content in the molten steel being controlled within $(38 \pm 2) \times 10^{-6}$, it is considered that the change of oxygen content in H13 castings is caused by the distribution of oxygen inclusions. Therefore, the statistical analysis position of oxide inclusion size distribution can be determined according to the oxygen content at each position.

3.2.1 Determination of analysis position of oxide inclusions in H13 castings

After solidification in the super-gravity field, the oxygen content at each position of castings A, B, and C is shown in Fig. 4. When the rotation radius is equal to 0.220 m, the oxygen content in the three castings is basically the same, and its value is about 40×10^{-6}. The reason is that a small amount of molten steel will cool rapidly after entering the casting mold, resulting in the solidification of molten steel before the oxide inclusions in the molten steel are removed.

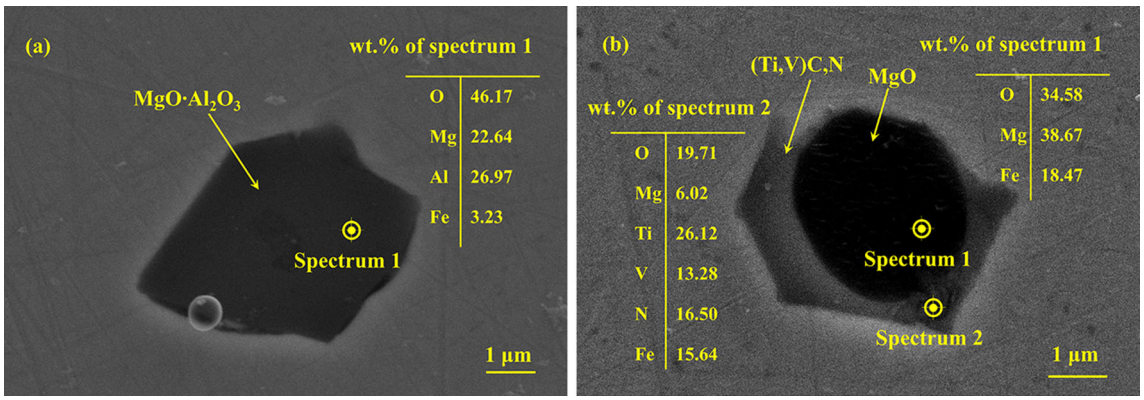

Fig. 3 Types of oxide inclusions in H13 castings under super-gravity field with multi-rotation speeds. **a** Magnesia–aluminum spinel; **b** composite inclusions of MgO and (Ti, V)C,N

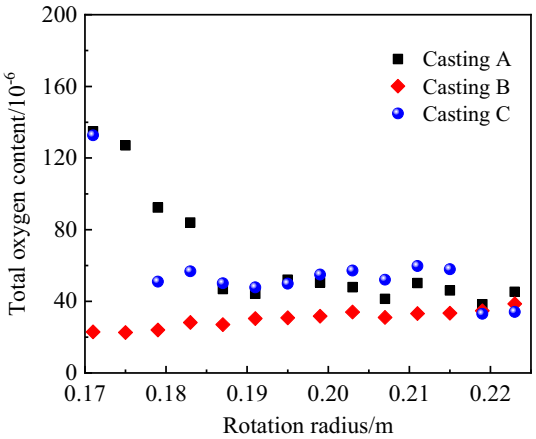

Fig. 4 Total oxygen content at each position of castings A, B, and C

When the rotation radius is in the range of 0.185–0.225 m, with the decrease in the rotation radius, the total oxygen content at each position of castings A and C fluctuates in the range of 40×10^{-6}–60×10^{-6}; when the rotation radius is in the range of 0.170–0.185 m, the total oxygen content at each position of castings A and C increases with the decrease in rotation radius. When the rotation radius is in the range of 0.170–0.225 m, the total oxygen content at each position of casting B decreases with the decrease in rotation radius. Based on the above analysis, three positions where rotation radius is equal to 0.21, 0.19, and 0.17 m, namely the outer, middle, and inner positions, are selected to analyze the influence of super-gravity on the size and quantity of oxide inclusions.

3.2.2 Statistics on size and quantity of oxide inclusions in H13 castings

The characteristics of oxide inclusions in the outer, middle, and inner positions of castings A, B, and C were counted using an INCA particle automatic analysis system. The selected scanning area is 4 mm × 4 mm, and the minimum length of statistical oxide inclusion is 1 μm.

The quantity and total area of oxide inclusions at the outer, middle, and inner positions of castings A, B, and C are shown in Fig. 5. It can be seen from Fig. 5a that the relationship between the quantity of oxide inclusions in castings A, B, and C and the rotation radius is different. With the decrease in rotation radius, the quantity of oxide inclusions in castings A and B decreases, while the quantity of oxide inclusions in casting C first increases and then decreases slightly. In combination with Fig. 4, it can be found that the variation trend of the quantity of oxide inclusions with the rotation radius is inconsistent with that of the total oxygen content with the rotation radius. Therefore, the quantity of oxide inclusions is not the direct reason affecting the total oxygen content. Figure 5b shows the relationship between the area occupied by oxide inclusions and the rotation radius in castings A, B, and C. It can be seen that in castings A and C, the area occupied by the outer and middle oxide inclusions is basically the same, while the area occupied by the inner oxide inclusions increases significantly. The area occupied by oxide inclusions at the outer, middle, and inner positions of casting B decreases in turn. The statistical results are consistent with the variation trend of total oxygen content with rotation radius, indicating that the difference in the size of oxide inclusions at each position is the direct reason for the difference in total oxygen content.

The size and quantity distribution of oxide inclusions in castings A, B, and C are shown in Fig. 6. It can be seen that in the three castings, the proportion of oxide inclusions with a length of less than 10 μm can exceed 80%. At the outer position of the castings, the proportion of oxide inclusions with a length greater than 10 μm in castings A and C is less than 10%, while the proportion of oxide inclusions with a length greater than 5 μm in casting B is less than 10%. At the middle position of the castings, the

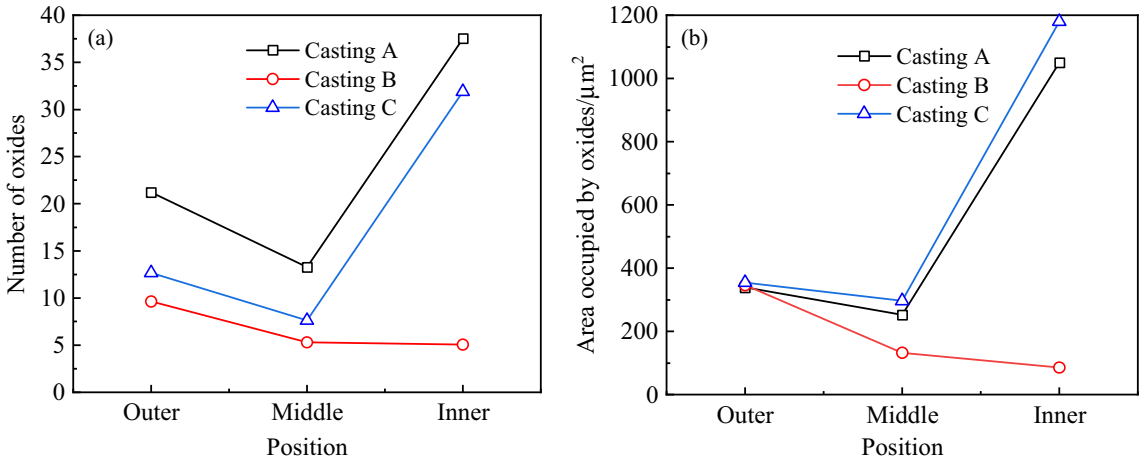

Fig. 5 Number of oxide inclusions (**a**) and area occupied by oxide inclusions (**b**) at outer, middle, and inner positions of castings A, B, and C

length of oxide inclusions in castings A, B, and C is all less than 10 μm, and the oxide inclusions with a length of less than 5 μm in casting B account for the highest proportion, which exceeds 85%. At the inner position of the castings, the proportion of oxide inclusions with a length greater than 10 μm in castings A and C is more than 15%, and the proportion of oxide inclusions with a length greater than 5 μm in casting B is less than 20%.

The size distribution of oxide inclusions at the outer position of castings A, B, and C is shown in Fig. 6a and b. The length of oxide inclusions in casting A is concentrated in the range of 5–10 μm, and the quantity of oxide inclusions in this length range is 11, which accounts for 70%. The length of oxide inclusions in casting B is concentrated in the range of 2–5 μm, and the quantity of oxide inclusions in this length range is 28, which accounts for 75%. The length of oxide inclusions in casting C is concentrated in the range of 2–10 μm, of which there are 12 oxide inclusions with lengths ranging from 2–5 and 5–10 μm, each accounting for 40%. In summary, it can be shown that at the outer position of the castings, compared with castings A and C, although the quantity of oxide inclusions in casting B is larger, the size is smaller.

The size distribution of oxide inclusions at the middle position of castings A, B, and C is shown in Fig. 6c and d. The length of oxide inclusions in casting A is concentrated in the range of 2–10 μm, of which there are 10 oxide inclusions with lengths ranging from 2–5 and 5–10 μm, each accounting for 50%. The length of oxide inclusions in casting B is concentrated in the range of 1–2 μm, and the quantity of oxide inclusions in this length range is 18, which accounts for 65%. The length of oxide inclusions in casting C is concentrated in the range of 2–5 μm, and the quantity of oxide inclusions in this length range is 31, which accounts for 70%. In summary, it can be shown that at the middle position of the castings, the oxide inclusions in casting B are less in quantity and smaller in size compared with castings A and C.

The size distribution of oxide inclusions at the inner position of castings A, B, and C is shown in Fig. 6e and f. 50% of the oxide inclusions in casting A are concentrated in the length of 5–10 μm, and the length of oxide inclusions larger than 10 μm accounts for 20%. The length of oxide inclusions in casting B is concentrated in the range of 2–5 μm, and the quantity of oxide inclusions in this length range is 11, which accounts for 65%. In addition, the maximum length range of oxide inclusions in casting B is 5–10 μm, which only accounts for 10%. 70% of the oxide inclusions in casting C are concentrated in the length of 5–10 μm, and the length of oxide inclusions larger than 10 μm accounts for about 20%. In summary, it can be shown that at the inner position of the castings, the oxide inclusions in casting B are less in quantity and smaller in size compared with castings A and C.

Previous studies have shown that the removal rate of oxide inclusion is positively correlated with the super-gravity coefficient, that is, a large super-gravity coefficient is beneficial to the removal of inclusions [24]. The definition of the super-gravity coefficient [25, 26] is given in Eq. (1).

$$G = \frac{\sqrt{g^2 + (\omega^2 R)^2}}{g} = \frac{\sqrt{g^2 + \left(\frac{N^2\pi^2 R}{900}\right)^2}}{g} \quad (1)$$

where ω is the angular speed, rad/s; N is the rotation speed, r/min; R is the distance between the center of rotation and the observation position (i.e., rotation radius), m; and g is the normal gravitational acceleration, $g = 9.8$ m/s^2.

According to Eq. (1), it can be found that when the observation position is the same, the super-gravity coefficient of casting C is the largest. However, according to the statistical results on the size distribution at the outer,

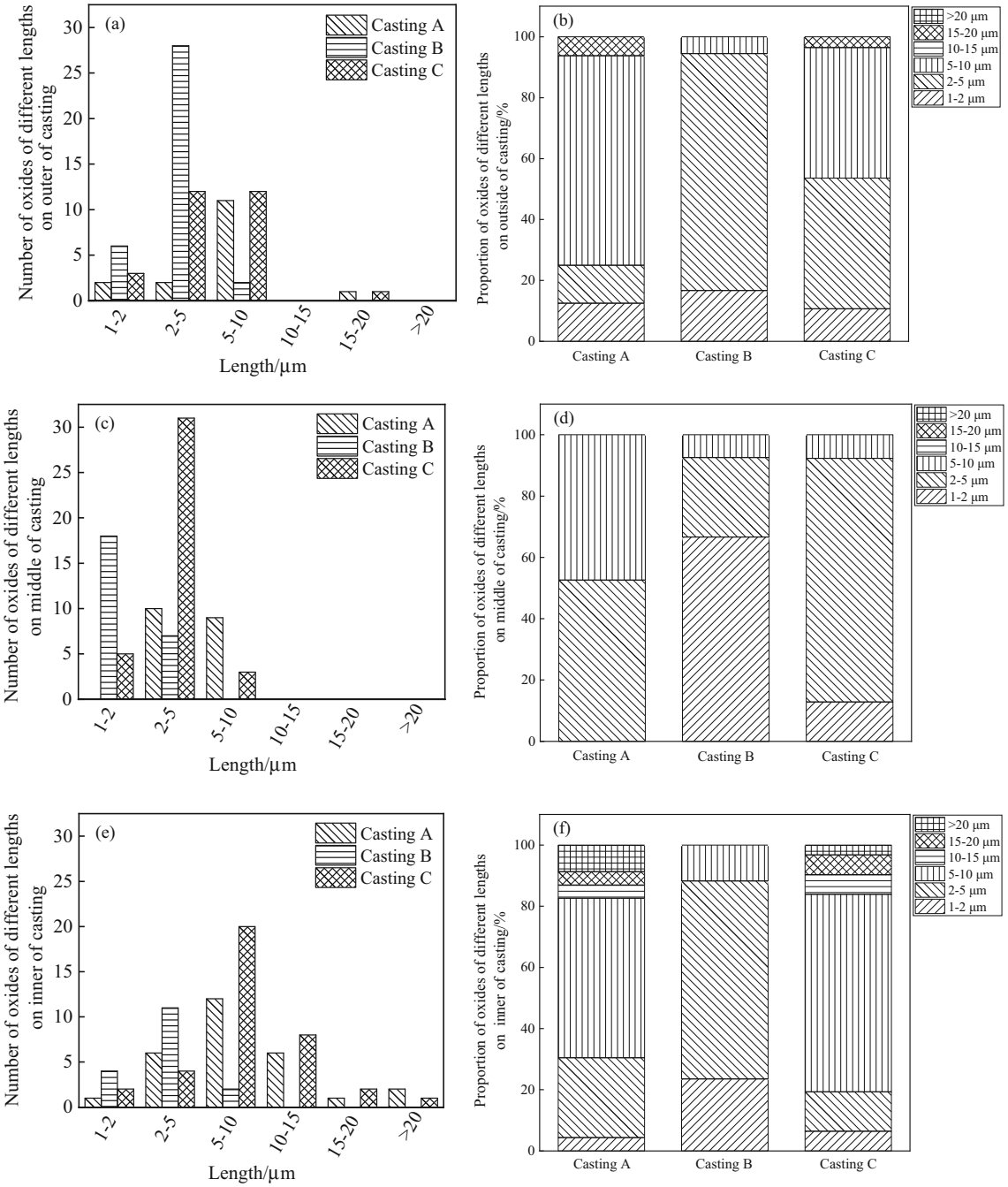

Fig. 6 Size of oxide inclusions at different positions in castings A, B, and C

middle, and inner position of castings A, B, and C, it can be found that the quantity and size of oxide inclusions in casting B are the least. Obviously, the research results are inconsistent with those of previous studies. Therefore, the influence mechanism of super-gravity on the distribution of oxide inclusions under the experimental conditions of this study will be discussed below.

4 Discussion

As a method to remove oxide inclusion in molten steel, super-gravity metallurgy has attracted the attention of metallurgical scholars. Previous studies have conducted a large number of laboratory simulation experiments on the removal mechanism of oxide inclusion by super-gravity [22, 24]. The super-gravity solidification castings in these simulation experiments are small in size, and the cooling

rate in the solidification process can be well controlled. However, in the industrial production process of super-gravity castings, it is difficult to control the cooling rate of solidification process. Therefore, the mechanism of super-gravity purification of molten steel in industrial process is different from that in laboratory-scale experiments. In this section, the distribution mechanism of oxide inclusions in the castings under different super-gravity solidification conditions was discussed from four aspects: (i) the formation temperature of oxide inclusions, (ii) the flow state of oxide inclusions in molten steel, (iii) the removal time of oxide inclusions, and (iv) the solidification time of molten steel.

4.1 Theoretical formation temperature of oxide inclusions

The relationship between the formation Gibbs free energy of possible oxide inclusions in the castings and the molten steel temperature is shown in Fig. 7. The liquidus temperature of H13 casting is 1470 °C, and thus, the calculation range of molten steel temperature is set as 1470–2100 °C. In this temperature range, the formation Gibbs free energy of oxide inclusion decreases with the decrease in molten steel temperature. And only the formation Gibbs free energy of MgO and Al_2O_3 has an intersection with the dotted line, where ΔG is equal to 0, and the corresponding formation temperatures are 1705 and 1600 °C, respectively, indicating that only MgO and Al_2O_3 are formed in the liquid phase.

4.2 Flow state of oxide inclusions in molten steel

The densities of MgO and Al_2O_3 inclusions are 3.58 and 3.97 g cm^{-3}, respectively, which are less than the density of molten steel [27]. Under the action of super-gravity, oxide inclusions and molten steel will produce two different movement speeds. Each casting is located in the

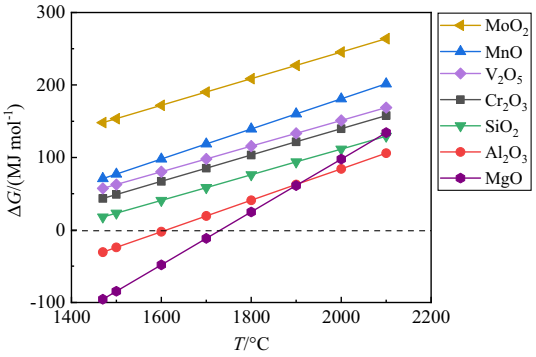

Fig. 7 Relationship between formation Gibbs free energy of possible oxide inclusions in castings and molten steel temperature T

super-gravity field with different rotation parameters, and the centrifugal force on the oxide inclusion in each casting and the centrifugal force on the molten steel are also different, which leads to the inward movement of the oxide inclusion relative to the molten steel.

In the solidification process of super-gravity field, the inward movement state of oxide inclusion includes the inward movement of oxide inclusion itself, the collision between oxide inclusions, and the adsorption of oxide inclusion by the wall [28], in which the mutual collision and agglomeration growth between oxide inclusions are the main way for the inward movement of oxide inclusions [29]. Previous research results show that the turbulent shear collision of oxide inclusions is the main collision mode of oxide inclusions [30], which is closely related to the flow state of molten steel.

Figure 8 shows the collision and agglomeration mode of oxide inclusions under different flow states of molten steel. The black line circle on the outside in Fig. 8 represents the mold, and the arrow on the black line circle represents the rotation direction of the mold. The red dotted line represents the pure molten steel after slag–steel separation, and the red dotted line and orange ring represent the mixture of molten slag and molten steel. The red arrow and black arrow represent the direction of centrifugal force on the molten steel and oxide inclusions, respectively. The black solid line circle indicates the starting position of oxide inclusion, the black dotted circle with arrow indicates the oxide inclusion during movement, and the black dotted circle indicates the oxide inclusion after movement. Figure 8a shows the collision mode of oxide inclusions in laminar flow. It can be seen that the movement of molten steel and slag is regular, the flow is layered, and the rotating flow trajectory is smooth. Under the action of centrifugal force, some oxide inclusions collide and grow up, and orderly gather in the center of the centrifugal circle, so as to enter the slag and purify the molten steel. Compared with Fig. 8a, the molten steel and slag in Fig. 8b are in a transitional flow state between laminar flow and turbulence, and the trajectory of rotating flow fluctuates slightly. Under this interference, the collision between oxide inclusions intensifies, which strengthens the purification effect of super-gravity on molten steel. The molten steel and slag in Fig. 8c are in a turbulent state. In this state, the flow of molten steel and slag is very irregular. Affected by the turbulent shear force, the oxide inclusions are more likely to collide and move into the slag, so as to purify the molten steel.

In the super-gravity field, Reynolds number (Re) is an important parameter to judge the inward movement state of oxide inclusion, and its expression is shown in Eq. (2) [31, 32].

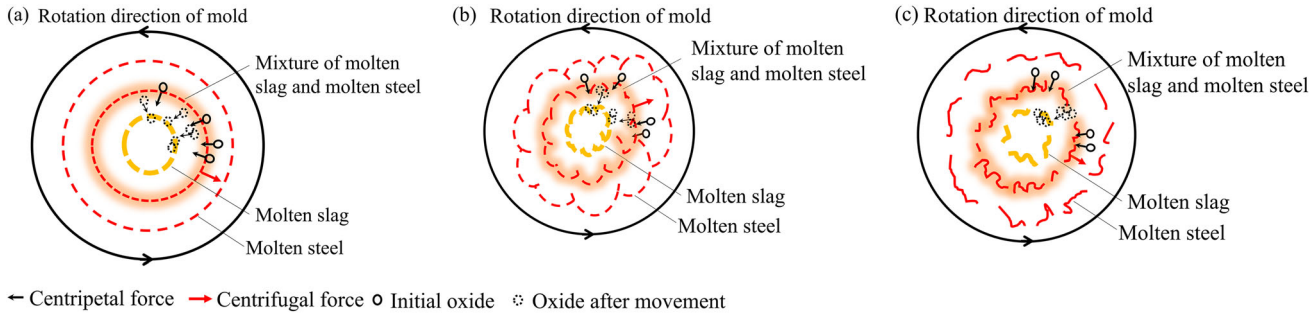

Fig. 8 Schematic diagram of motion trajectory of oxide inclusion under different flow states. **a** Steady flow; **b** transition flow; **c** turbulence

$$Re = \frac{du}{\eta} \tag{2}$$

where d is the diameter of oxide inclusion, m; η is the dynamic viscosity of molten steel, with a value of 8×10^{-7} m^2 s^{-1}; and u is the separation velocity of oxide inclusions, m s^{-1}.

In the solidification process of super-gravity field, the separation speed of oxide inclusions is affected by the density difference between molten steel and oxide inclusions. Under the super-gravity experimental conditions in this study, the super-gravity is much greater than the resultant force of the oxide inclusion's own gravity and the buoyancy force, and thus, the effect of the resultant force on the motion trajectory of the oxide inclusion is ignored in this study. In addition, uncommon forces such as pressure gradient force, Brown force, and Basset force are also ignored [33]. Therefore, this study considers that the oxide inclusions move in a straight line from the outer edge of the casting to the rotation center, and the motion rule of the oxide inclusions in molten steel follows Stokes formula [34, 35], as shown in Eq. (3).

$$u' = \frac{d^2(\rho_m - \rho_s)}{18\eta}\omega^2 r \tag{3}$$

where u' is the movement rate of oxide inclusion in molten steel under the action of super-gravity; ρ_m is the density of molten steel, which is 7.1×10^3 kg m^{-3}; ρ_s is the density of inclusions. Since the density of MgO inclusions is similar to that of Al_2O_3 inclusions, the density of Al_2O_3 inclusions is selected for theoretical calculation, and ρ_s is 3.97×10^3 kg m^{-3}; and r is the distance between the oxide inclusion and the rotation center, m.

The relationship between Reynolds number and rotation radius of inward movement of oxide inclusions with different particle sizes in castings A, B, and C is shown in Fig. 9. According to the Reynolds number, the flow state can be divided into three types [36]. Among them, when $Re < 2300$, the flow is laminar, as shown in the gray area in Fig. 9; when $Re > 4000$, the flow is turbulent, as shown in the yellow area in Fig. 9; when $2300 < Re < 4000$, the flow is transitional, as shown in purple in Fig. 9. For casting A, it can be seen from Fig. 9a that when the rotation radius is constant, the Reynolds number of the inward movement of the oxide inclusion increases with the increase in the diameter of the oxide inclusion; when the particle size of oxide inclusion is constant, the Reynolds number of the inward movement decreases with the decrease in the rotation radius of oxide inclusion. Compared with large-size oxide inclusions, the rotation radius of small-size oxide inclusions has little effect on the Reynolds number. In addition, in casting A, when the rotation radius is greater than 0.2 m, only the oxide inclusions with a particle size greater than 20 μm are in a turbulent state; oxide inclusions with a particle size less than 15 μm are in a laminar flow state. Figure 9b shows the relationship between Reynolds number and rotation radius of inward movement of oxide inclusions with different particle sizes in casting B. Compared with casting A, the rotation speed of casting B in the super-gravity field increases stepwise. Therefore, when the particle size of oxide inclusions is constant, the Reynolds number changes nonlinearly with the rotation radius. However, when the rotation radius is constant, the Reynolds number of the inward movement increases with the increase in the particle size of oxide inclusions. In addition, oxide inclusions with a particle size of 5 and 10 μm in casting B are in a laminar flow state, oxide inclusions with a particle size of 15 μm are in a transitional flow state, and oxide inclusions with a particle size of 20 μm are in a turbulent flow state. The relationship between Reynolds number and rotation radius of inward movement of oxide inclusions with different particle sizes in casting C is similar to that in casting B, as shown in Fig. 9c. When the rotation radius is the same, the Reynolds number of oxide inclusions with particle size of 15 and 20 μm in casting C is greater than that of casting B, and the Reynolds number is greater than 4000, which is in a turbulent state.

In summary, from the perspective of the flow state of oxide inclusions in molten steel, it can be found that increasing the particle size of oxide inclusions and the

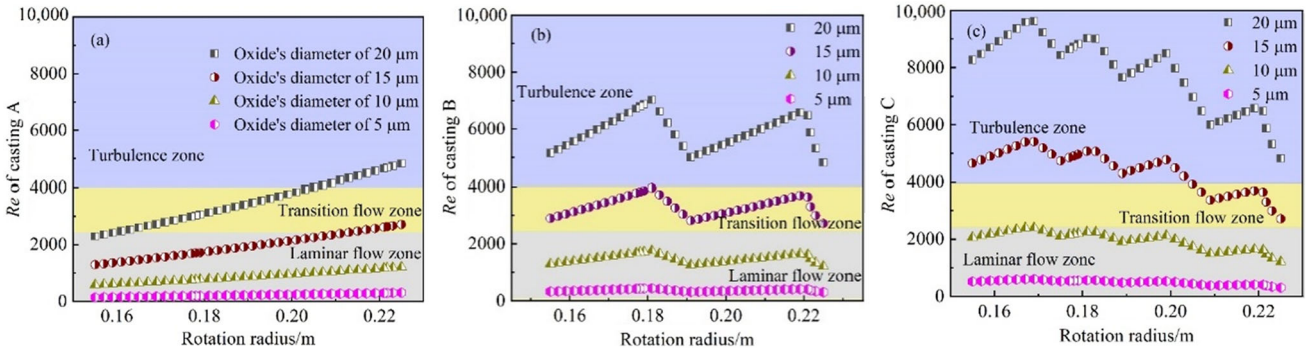

Fig. 9 Relationship between inward movement Reynolds number of oxide inclusions with different particle sizes and rotation radii in castings. **a** Casting A; **b** casting B; **c** casting C

rotation speed in super-gravity field is beneficial to the removal of oxide inclusions. If only from this perspective, the removal effect of oxide inclusions in casting A is the worst, and the removal effect of oxide inclusions in casting C is the best. However, this conclusion is inconsistent with the statistical results in Fig. 6. Therefore, in addition to the flow state of oxide inclusions in molten steel, there are other factors that affect the removal effect of oxide inclusions.

4.3 Comparison between solidification time of molten steel and inward movement time of oxide inclusions

The solidification time of molten steel and the inward movement time of oxide inclusions are also important factors affecting the number of oxide inclusions in steel. In the experimental process of this study, a small amount of slag first enters the super-gravity field, the mixture of slag and molten steel then enters the super-gravity field, and the slag at the bottom of the ladle finally enters the super-gravity field. A small amount of molten slag rapidly solidifies in the super-gravity field to form a slag crust. Because there is a certain density difference between molten slag and molten steel, the molten slag moves centripetally relative to molten steel under the action of super-gravity. Therefore, a large amount of molten slag moves to the center of the super-gravity field, while a large amount of molten steel moves to the outside of the super-gravity field, which forms a super-gravity field with high center temperature and low edge temperature. And the solidification time of molten steel at each position in the super-gravity field is different. In order to simplify the calculation process, the molten steel with a thickness of 2 mm is taken as the research object, as shown in Fig. 10a. Assuming that the initial position of the oxide inclusions is on the outside, under the action of super-gravity, the time required for the oxide inclusions to move inward to the inside of 2 mm thick molten steel is called the inward movement time of the oxide inclusions, and the solidification time of 2 mm thick molten steel is called the solidification time of molten steel. When the solidification time of the molten steel is greater than the inward movement time of oxide inclusions, the oxide inclusions can completely move inward, and the oxide inclusions are removed at this time, as shown in Fig. 10b. When the solidification time of the molten steel is less than the inward movement time of the oxide inclusions, the oxide inclusions cannot completely move inward from the molten steel. At this time, the oxide inclusions are solidified in the steel and cannot be removed, as shown in Fig. 10c.

According to previous research, the relationship between secondary dendrite spacing of H13 steel and local cooling rate can be expressed by Eq. (4) [37].

$$\lambda_2 = 175.4 R_C^{-0.322} \tag{4}$$

where λ_2 is the secondary dendrite spacing, μm; and R_C is the local cooling rate, °C min^{-1}.

Since the secondary dendrite spacing at each position is different, the local cooling rate at each position in the super-gravity casting can be calculated according to Eq. (4). Therefore, the solidification time of molten steel $t_{solidify}$ can be expressed by Eq. (5).

$$t_{solidify} = \frac{T_j - T_{0.5\ s}}{R_C} \tag{5}$$

where T_j is the casting temperature of molten steel, which is 1520 °C; since the oxide inclusion is difficult to move inward when the solid fraction in molten steel exceeds 50% [24], the solidification temperature is determined as the molten steel temperature when the solid fraction is 50%, which is recorded as $T_{0.5\ s}$. According to Ref. [38], the value of $T_{0.5\ s}$ is set as 1430 °C.

Combining Eqs. (4) and (5), Eq. (6) can be obtained.

$$t_{solidify} = \frac{90}{\left(\frac{\lambda_2}{175.4}\right)^{-3.11}} \tag{6}$$

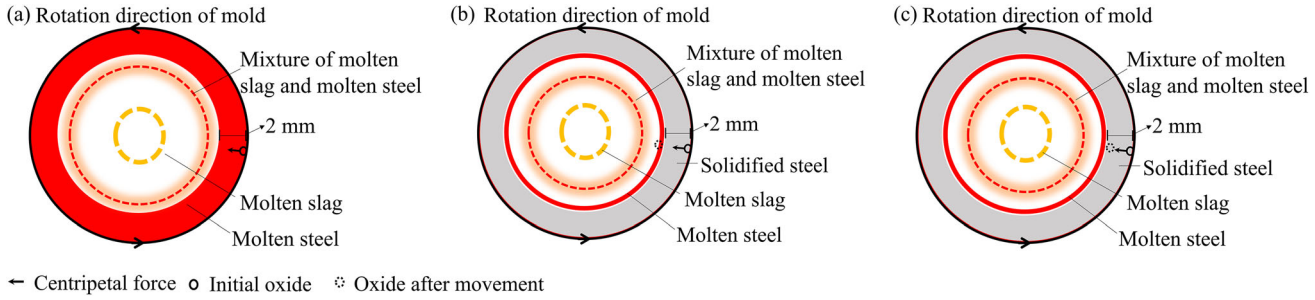

Fig. 10 Inward movement of oxide inclusions under different solidification time. **a** Molten steel has not yet solidified; **b** solidification time of molten steel is greater than inward movement time of oxide inclusions; **c** solidification time of molten steel is less than inward movement time of oxide inclusions

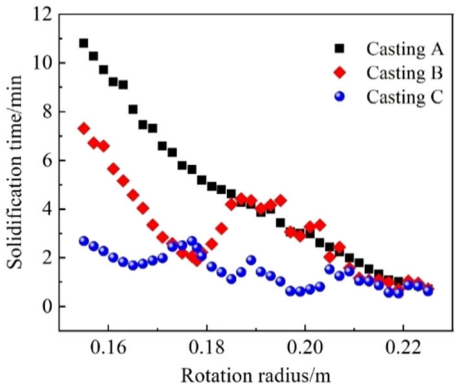

Fig. 11 Solidification time of molten steel at each position in castings A, B, and C

Combined with the statistical results of secondary dendrite spacing at different positions of different tool rings (as shown in Fig. 6a in Ref. [38]), the solidification time of the molten steel at each position in castings A, B, and C can be calculated, as shown in Fig. 11.

It can be seen from Fig. 11 that the solidification time of the molten steel in casting A increases with the decrease in the rotation radius. When the rotation radius is in the range of 0.185–0.225 m, the solidification time of the molten steel in casting B is basically the same as that in casting A, while the solidification time of the molten steel in casting B is less than that in casting A when the rotation radius is in the range of 0.155–0.185 m. Compared with castings A and B, the solidification time of the molten steel in casting C is shorter in the range of 0.155–0.210 m. The calculation results show that the solidification time of the molten steel in casting A is the longest, which provides favorable conditions for the inward movement of oxide inclusions.

In addition to the solidification time of molten steel, the distribution of oxide inclusions in super-gravity casting is also affected by the inward movement time (t_{remove}) of oxide inclusions. The calculation of t_{remove} can be expressed by Eq. (7).

$$\frac{\mathrm{d}R}{\mathrm{d}t_{\text{remove}}} = u' \tag{7}$$

Combining Eqs. (3) and (7), Eq. (8) can be obtained.

$$\frac{\mathrm{d}R}{\mathrm{d}t_{\text{remove}}} = \frac{d^2(\rho_{\text{m}} - \rho_{\text{s}})}{18\eta}\omega^2 r \tag{8}$$

Simplifying Eq. (8), Eq. (9) can be obtained.

$$t_{\text{remove}} = \frac{900 \times 18\eta}{d^2(\rho_{\text{m}} - \rho_{\text{s}})\pi^2 N^2} \ln\frac{R}{R - 0.002} \tag{9}$$

The inward movement time of oxide inclusions with different particle sizes in castings A, B, and C can be calculated by using Eq. (9), and the results are shown in Fig. 12.

The difference (t_{D}) between the solidification time of molten steel and the inward movement time of oxide inclusions with different particle sizes is an important index indicating whether the oxide inclusions can be completely inwardly moved, as shown in Eq. (10).

$$t_{\text{D}} = t_{\text{solidify}} - t_{\text{remove}} \tag{10}$$

If t_{D} is greater than zero, it means that the oxide inclusions can be completely removed before the molten steel is completely solidified, and the molten steel begins to solidify, which means that the molten steel can be completely purified. If t_{D} is less than zero, it means that the molten steel has solidified before the movement of oxide inclusions is completed, which means that the oxide inclusions have not been completely removed and the molten steel has not been effectively purified. According to Eq. (10), the time difference between the solidification time of molten steel at different positions in castings and the inward movement time of oxide inclusions with different particle sizes can be calculated, and the results are shown in Fig. 13.

At $t_{\text{D}} = 0$, there is a zero-tick mark. The point above the zero-tick mark indicates that the oxide inclusion can be completely moved inward, and the point below the zero-tick mark indicates that the oxide inclusion cannot be

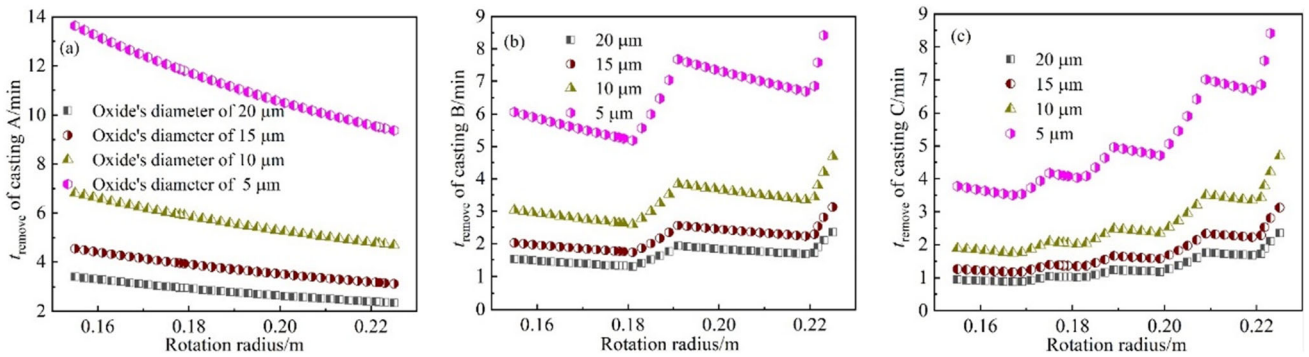

Fig. 12 Inward movement time of oxide inclusions with different particle sizes in castings. **a** Casting A; **b** casting B; **c** casting C

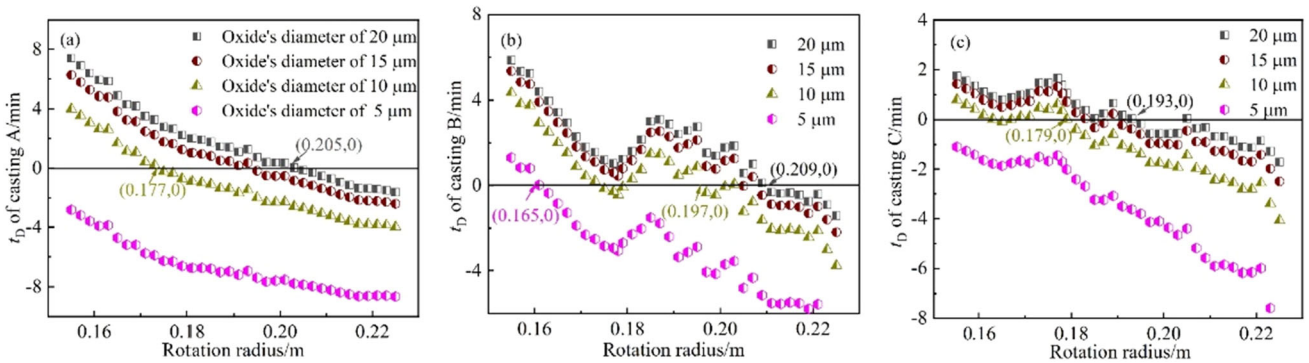

Fig. 13 Time difference between solidification time of molten steel at different positions in castings and inward movement time of oxide inclusions with different particle sizes. **a** Casting A; **b** casting B; **c** casting C

completely moved inward. In casting A, the inward movement effect of oxide inclusion increases with the decrease in rotation radius, and the oxide inclusions with particle sizes of 20, 15, and 10 μm can be effectively moved inward in the range of 0.155 m $< R <$ 0.205 m, 0.155 m $< R <$ 0.196 m and 0.155 m $< R <$ 0.177 m, respectively, while the oxide inclusions with a particle size of 5 μm cannot be completely moved inward, as shown in Fig. 13a.

As the super-gravity field rotation speed of casting B gradually increases, the inward movement effect of oxide inclusions in casting B changes with the decrease in the rotation radius. In the range of 0.155 m $< R <$ 0.179 m and 0.186 m $< R <$ 0.225 m, the inward movement effect of oxide inclusions increases with the decrease in the rotation radius, while in the range of 0.179 m $< R <$ 0.186 m, the inward movement effect of oxide inclusions decreases with the decrease in the rotation radius, as shown in Fig. 13b. Compared with the casting A, the effective inward movement range of oxide inclusions in casting B is significantly increased. The oxide inclusions with particle sizes of 20, 15, 10, and 5 μm can be effectively moved inward in the range of 0.155 m $< R <$ 0.209 m, 0.155 m $< R <$ 0.205 m, 0.155 m $< R <$ 0.197 m, and 0.155 m $< R <$ 0.165 m, respectively.

Compared with the castings A and B, the effective inward movement range of oxide inclusions in casting C is the smallest. As shown in Fig. 13c, the oxide inclusions with particle sizes of 20, 15, and 10 μm can be effectively moved inward in the range of 0.155 m $< R <$ 0.193 m, 0.155 m $< R <$ 0.191 m, and 0.155 m $< R <$ 0.165 m and 0.172 m $< R <$ 0.179 m, respectively, while the oxide inclusions with a particle size of 5 μm cannot be completely moved inward.

The theoretical analysis results show that among the three castings A, B, and C, the effective inward movement range of oxide inclusions in casting B is the largest, and the purification effect of molten steel is the best. This result is consistent with the statistical results of oxide inclusions in castings A, B, and C. In addition, it can be seen from the analysis results that for any casting, the inward movement effect of oxide inclusions on the inside of the casting is the best among the three analysis positions, which is inconsistent with the statistical results in Fig. 6. The reason is that although the t_D value inside the casting is large, the *Re* value is relatively small, which is not conducive to the collision and growth of oxide inclusions, resulting in the number of oxide inclusions at the inner positions of the casting greater than that in the middle positions of the casting. In summary, the distribution of oxide inclusions in

super-gravity castings is affected by the movement state of oxide inclusions in molten steel, the solidification time of molten steel, and the inward movement time of oxide inclusions.

5 Conclusions

1. In the range of $0.185\ \text{m} < R < 0.225\ \text{m}$, the total oxygen content at each position in the super-gravity castings with constant rotation speed and five-stage rotation speeds fluctuates within the range of 40×10^{-6}–60×10^{-6}. In the range of $0.170\ \text{m} < R < 0.185\ \text{m}$, the total oxygen content in the super-gravity castings with constant rotation speed and five-stage rotation speeds increases with the decrease in the rotation radius. In the range of $0.170\ \text{m} < R < 0.225$ m, the total oxygen content at each position in super-gravity casting with three-stage rotation speeds decreases with the decrease in the rotation radius.
2. The oxide inclusions with a particle size greater than 10 μm are mainly concentrated at the inner and outer positions in the super-gravity casting with constant rotation speed and five-stage rotation speeds, and the number of oxide inclusions with a particle size greater than 10 μm at the inner position is greater than that at the outer position. At the inner position in the super-gravity casting with constant rotation speed and five-stage rotation speeds, the number of oxide inclusions with a particle size greater than 10 μm is 11 and 12, accounting for 18% and 16%, respectively. There is no oxide inclusion with a particle size greater than 10 μm at the outer, middle, and inner positions of the super-gravity casting with three-stage rotation speeds.
3. An increase in the particle size of oxide inclusion and rotation speed in super-gravity field is conducive to the collision and growth of oxide inclusions in molten steel, thereby shortening the inward movement time of oxide inclusions. However, increasing the rotation speed in the super-gravity field shortens the solidification time of molten steel, which is not conducive to the inward movement of oxide inclusions. Therefore, in the rotation speed range of the super-gravity field studied in this paper, the composite super-gravity field with three-stage rotation speeds has the best effect on the removal of oxide inclusions in molten steel.

Acknowledgements This work was financially supported by China Postdoctoral Fund (No. 2021M700394) and Key R&D Plan of Shandong Province in 2021 (No. 2021CXGC010209). The authors thank the Beijing Key Laboratory of Special Melting and Preparation of High-end Metal Materials for its support. The authors wish to thank the timely help given by Li-hui Han in University of Science and Technology Beijing.

Conflict of interest The authors declare no conflict of interest.

References

[1] J. Zhu, Z.H. Zhang, J.X. Xie, Mater. Sci. Eng. A 752 (2019) 101–114.
[2] C. Meng, H. Zhou, H.F. Zhang, X. Tong, D.L. Cong, C.W. Wang, L.Q. Ren, Mater. Des. 51 (2013) 886–893.
[3] C.B. Shi, ISIJ Int. 60 (2020) 1083–1096.
[4] C.B. Shi, X.C. Chen, H.J. Guo, Z.J. Zhu, H. Ren, Steel Res. Int. 83 (2012) 472–486.
[5] C.B. Shi, J.S. Wang, J. Li, J.W. Cho, J. Iron Steel Res. Int. 28 (2021) 1483–1503.
[6] K.Y. Miao, M. Nabeel, N. Dogan, S. Sun, Metall. Mater. Trans. B 52 (2021) 3151–3166.
[7] L.T. Wang, Q.Y. Zhang, S.H. Peng, Z.B. Li, ISIJ Int. 45 (2005) 331–337.
[8] Z. Taslicukur, C. Balaban, N. Kuskonmaz, J. Eur. Ceram. Soc. 27 (2007) 637–640.
[9] L. Zhang, S. Taniguchi, Int. Mater. Rev. 45 (2000) 59–82.
[10] Y. Miki, H. Kitaoka, T. Sakuraya, T. Fujii, ISIJ Int. 32 (1992) 142–149.
[11] Y. Miki, S. Ogura, T. Fujii, Kawasaki Steel Tech. Rep. (1996) No. 35, 67–73.
[12] Y. Kusano, Y. Kawauchi, M. Wajima, K. Sugawara, M. Yoshida, H. Hayashi, ISIJ Int. 36 (1996) S77–S80.
[13] X.F Zheng, P.C Hayes, H.G. Lee, ISIJ Int. 37 (1997) 1091–1097.
[14] A. Weidner, D. Krewerth, B. Witschel, M. Emmel, A. Schmidt, J. Gleinig, O. Volkova, C.G. Aneziris, H. Biermann, Steel Res. Int. 87 (2016) 1038–1053.
[15] A. Das, A. Bhowal, S. Datta, Ind. Eng. Chem. Res. 47 (2008) 4230–4235.
[16] C.C. Lin, K.S. Chien, Separ. Purif. Technol. 63 (2008) 138–144.
[17] Y.S. Chen, F.Y. Lin, C.C. Lin, C.Y.D. Tai, H.S. Liu, Ind. Eng. Chem. Res. 45 (2006) 6846–6853.
[18] T. Liu, Z.C. Guo, Z. Wang, M.Y. Wang, Appl. Surf. Sci. 256 (2010) 6634–6640.
[19] M.Y. Wang, Z. Wang, Z.C. Guo, Z.J. Li, Int. J. Hydrogen Energy 36 (2011) 3305–3312.
[20] C. Li, J.T. Gao, Z.C. Guo, Metall. Mater. Trans. B 47 (2016) 1516–1519.
[21] L.X. Zhao, Z.C. Guo, Z. Wang, M.Y. Wang, Metall. Mater. Trans. B 41 (2010) 505–508.
[22] G.Y. Song, B. Song, Y.H. Yang, Z.B. Yang, W.B. Xin, Metall. Mater. Trans. B 46 (2015) 2190–2197.
[23] C. Li, J.T. Gao, Z. Wang, Z.C. Guo, Metall. Mater. Trans. B 48 (2017) 900–907.
[24] G.Y. Song, B. Song, Z.B. Yang, Y.H. Yang, J. Zhang, Metall. Mater. Trans. B 47 (2016) 3435–3445.
[25] Y. Li, J.T. Gao, Z.L. Huang, Z.C. Guo, Ceram. Int. 45 (2019) 10961–10968.
[26] C. Li, J.T. Gao, Z. Wang, H.R. Ren, Z.C. Guo, ISIJ Int. 57 (2017) 767–769.
[27] U.D. Salgado, C. Weiß, S.K. Michelic, C. Bernhard, Metall. Mater. Trans. B 49 (2018) 1632–1643.
[28] X.C. Huang, B.K. Li, Z.Q. Liu, X. Yang, F. Tsukihashi, Int. J. Heat Mass Transfer 135 (2019) 1300–1311.
[29] M.Y. Zhu, W.T. Lou, W.L. Wang, Acta Metall. Sin. 54 (2018) 131–150.
[30] X.C. Chen, Development of a new process of induction electroslag centrifugal casting and its finite element simulation,

University of Science and Technology Beijing, Beijing, China, 2001.
[31] D.G. Zhao, M. Gao, X. Li, S.H. Wang, J. Iron Steel Res. 29 (2017) 32–38.
[32] W. Liu, S.F. Yang, J.S. Li, F. Wang, H.B. Yang, J. Iron Steel Res. Int. 26 (2019) 1147–1153.
[33] X.H. Wang, Ironmaking and steel metallurgy — steelmaking, Higher Education Press, Beijing, China, 2007.
[34] C. Li, Fundamental research on treatment of molten steel and steelmaking slag with super-gravity, University of Science and Technology Beijing, Beijing, China 2017.
[35] J.M. Du, Q.Z. Shen, Metallurgical transmission principle, Metallurgical Industry Press, Beijing, China, 2011.
[36] A. Kroupa, J. Havránková, M. Svoboda, M. Coufalová, J. Vřešt'ál, J. Phase Equilib. 22 (2001) 312.
[37] M.T. Mao, Investigation of precipitation and elimination of primary carbide in H13 steel, University of Science and Technology Beijing, Beijing, China, 2017.
[38] S.Y. Li, S.Y. Qin, X.J. Xi, G.Y. Sun, W.S. Yang, J. Guo, H.J. Guo, Metals 10 (2020) 1428.